CrossMark

A novel and facile way to synthesize vanadium pentoxide nanospike as cathode materials for high performance lithium ion batteries

Xiaowei Zhou [a], Chaojun Cui [b], Guangming Wu [a,*], Huiyu Yang [a], Jiandong Wu [a], Jichao Wang [a], Guohua Gao [a]

[a] Shanghai Key Laboratory of Special Artificial Microstructure Materials and Technology, Tongji University, Shanghai 200092, PR China
[b] Anyang Institute of Technology, Anyang 455000, PR China

HIGHLIGHTS

- VO_x-NTs are prepared by sol–gel method and hydrothermal treatment using dodecylamine as template.
- V_2O_5-NS consisting of interconnected V_2O_5 nanoparticles is obtained through sintering of VO_x-NTs.
- V_2O_5-NS exhibits superior electrochemical performance as cathode material for LIBs.

GRAPHICAL ABSTRACT
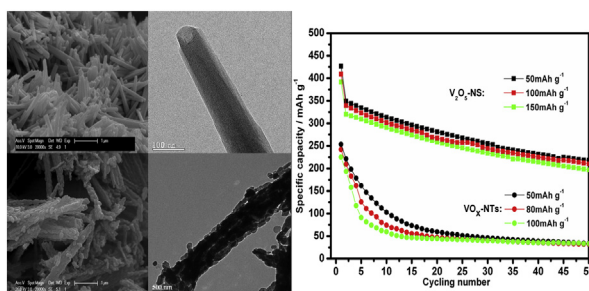
ARTICLE INFO

ABSTRACT

Vanadium oxide nanotubes (VO_x-NTs) are prepared by sol–gel method and subsequent hydrothermal treatment using dodecylamines as structure directing templates. After sintering of VO_x-NTs in the mixed gas flow of nitrogen and oxygen, we successfully obtain a kind of nanospike shaped vanadium pentoxide free of organic template. The synthesized vanadium pentoxide nanospike (V_2O_5-NS) is composed of interconnected V_2O_5 nanocrystals (50–200 nm) and exhibits superior specific capacity and cycling performance (427 mA h g^{-1} for the first cycle and 218 mA h g^{-1} after 50 cycles at 50 mA g^{-1} current density between 1.5 and 4 V versus Li/Li$^+$) when used as cathode materials for lithium ion batteries. Besides, V_2O_5-NS also possesses good rate capability. This novel method adopted in the work is facile and effective for the synthesis of nanostructured vanadium oxide.

© 2013 Elsevier B.V. All rights reserved.

1. Introduction

Lithium ion batteries (LIBs) are the preferable choices for energy storage devices such as portable electronics and electric vehicle, due to their high energy density, long cycle life and environmentally benign features [1,2]. Cathode materials used in LIBs have a

huge impact on their final electrochemical performances, and especially the bulk of the energy density in LIBs is contributed by the cathode [3]. The traditional cathode materials currently applied in LIBs only have a specific capacity in the range of 140 mA h g^{-1} to 170 mA h g^{-1}, such as $LiCoO_2$, $LiFePO_4$, etc. With increasing demand for high performance rechargeable LIBs, especially for high energy density and high rate capability applications, there is a pressing need for alternative high capacity cathode materials with higher energy density than traditional cathodes. Vanadium pentoxide (V_2O_5), which possesses several unique advantages such as low

cost, less toxicity and high energy density (its theoretical capacity is up to $\sim$440 mA h g^{-1} when three lithium ions are intercalated per V$_2$O$_5$ unit due to its special layered structure), has been extensively investigated and considered to be an attractive cathode candidate for LIBs [4–6]. However, the performance of bulk V$_2$O$_5$ powder cathode is limited by its intrinsic low diffusion coefficient of lithium ions ($\sim$10^{-12} cm^2 s^{-1}), poor electronic conductivity (10^{-2}–10^{-3} S cm^{-1}) and structural instability upon lithium intercalation/de-intercalation [7–9], resulting in low specific capacity, rapid capacity fading and poor rate capability. Many studies have shown that nanostructured materials can provide a new opportunity to solve these problems via increasing the electroactive surface area, shortening the lithium ion diffusion distance and absorbing mechanical stress associated with lithium ion intercalation/deintercalation owing to the small size derived from their nanometer morphology [10,11]. To improve the electrochemical performance of V$_2$O$_5$, there is an increasing interest in the fabricating of nanostructured vanadium oxide (e.g. nanotubes, nanowires, nanobelts, nanofibers, nanoflowers and nanorods) through various methods including sol–gel, hydrothermal treatment, reverse micelle technique, electrodeposition and electrospinning etc [10–16]. Among these methods, many usually involve severe conditions (e.g. high temperature and supercritical fluid), tedious procedures and sophisticated equipments [13–15]. Thus, a convenient and facile synthetic technique is vital to the practical and large scale applications of nanostructured vanadium oxide cathode materials.

In this work, first, vanadium oxide nanotubes (VO$_x$-NTs) are prepared through simple sol–gel process and hydrothermal treatment with dodecylamine as structure directing template [16], and then we introduce a facile and effective way to synthesize the novel nanospike shaped vanadium pentoxide cathode material for LIBs application by post sintering of VO$_x$-NTs in the mixed atmosphere of nitrogen and oxygen. The finally synthesized vanadium pentoxide nanospike (V$_2$O$_5$-NS) comprises interconnected nanoparticles and exhibits excellent initial capacity (427 mA h g^{-1}) and good cyclic performance (219 mA h g^{-1} after 50 cycles). Besides, when operating current increases, the electrochemical performance maintains well, which indicates V$_2$O$_5$-NS also possesses outstanding rate capability.

2. Experimental

2.1. Preparation of the samples

Firstly, 1.02 g crystalline V$_2$O$_5$ powder was slowly dissolved in a hydrogen peroxide solution (80 mL, 30%) under magnetic stirring about 30 min followed by strong exothermic reaction, which led to the formation of clear orange vanadium peroxide sol [17] and the release of oxygen, then the orange aqueous sol formed was aged for 3 days and gradually changed into a red gel. After 1.04 g dodecylamine (C$_{12}$H$_{25}$NH$_3^+$) was added to the red gel, the mixture was vigorously stirred for 24 h and transferred into a 100 mL Teflon-lined hydrothermal autoclave with a stainless steel shell. The autoclave was kept at 180 °C in a constant temperature oven for 5 days. The precipitate obtained was filtered, rinsed repeatedly with absolute ethanol and dried at 100 °C under vacuum for 8 h. The resulting black product was vanadium oxide nanotubes (VO$_x$-NTs). Finally, the as-prepared VO$_x$-NTs were sintered at 450 °C for 3 h in a mixed gas flow of nitrogen/oxygen (1:1 volume) with a heating rate of 2 °C min^{-1}. The synthesized yellow product was vanadium pentoxide nanospike (V$_2$O$_5$-NS).

2.2. Characterization of the samples

Field emission scanning electron microscopy (FESEM, Philips-XL-30FEG) and transmission electron microscopy (TEM, JEOL-1230) were employed to observe the morphology and structure of the samples. TEM powder samples were prepared by dispersing a drop of sample solution onto a copper wire mesh. X-ray powder diffraction (XRD) patterns were obtained by using a RigataD/max-C diffractometer with Cu Kα radiation source (λ = 1.5406Å). XPS experiments were conducted on a RBD upgraded PHI-5000C ESCA system (Perkin Elmer) with Mg Kα radiation ($h\nu$ = 1253.6 eV). Binding energies were calibrated by using the containment carbon (C$_{1s}$ = 284.6 eV). The data analysis was carried out by using XPS Peak4.1 software. The thermogravimetry (TG) and differential scanning calorimeter (DSC) measurements were performed on a SDT Q600 in the temperature range of 26–650 °C with a heating rate of 5 °C min^{-1} in air atmosphere. Fourier transform infrared (FTIR) spectra were collected with KBr pellets in the range of 400–4000 cm^{-1} using a Bruker-TENSOR27 FTIR spectrometer.

2.3. Electrode preparation and electrochemical measurements

Cathode materials were prepared by mixing 70% active materials (VO$_x$-NTs or V$_2$O$_5$-NS), 20% carbon black as conducting agent and 10% polyvinylidene fluoride (PVDF) as a binder in N-methyl-pyrrolidone (NMP) solvent. The viscous slurry was stirred thoroughly and subsequently coated on aluminum foil. The pasted cathode was dried at 120 °C for 8 h and then pressed. A microporous film (Celgard 2500) was used as the separator, lithium metal as the counter and reference electrode, and electrolyte was 1 M LiPF$_6$ dissolved in ethylene carbonate (EC)/dimethyl carbonate (DMC) (1:1 volume). The coin cells were assembled in an argon-filled glove box.

Galvanostatic charge/discharge tests were performed by using LAND cell-testing system between 1.5 and 4 V. Cyclic voltammetry (CV) was conducted over a potential range from 1.5 to 4.0 V with a scanning rate of 2 and 0.1 mV s^{-1} using CHI660C electrochemical workstation. Electrochemical impedance spectroscopy (EIS) was collected in the frequency range between 100 kHz and 0.01 Hz at a state of charge (SOC) of 3 V with 5 mV AC signal amplitude. Nyquist plots were fitted and analyzed using Zview software. All electrochemical tests were carried out at the room temperature ($\sim$25 °C).

3. Results and discussion

TEM images of VO$_x$-NTs in Fig. 1(a–d) show that VO$_x$-NTs consisting of alternately arranged VO$_x$ layers (dark fringes) and dodecylamine templates (broad fringes) have the open-ended multilayered tubular structure with the length of 1–3 μm and diameter of 100–200 nm. High magnification TEM image (Fig. 1d) indicates the distance between adjacent VO$_x$ layers is $\sim$3 nm, representing the approximate length of dodecylamine template. It can be seen from Fig. 1(e–h) that V$_2$O$_5$-NS synthesized through sintering of VO$_x$-NTs is composed of small interconnected nanoparticles with the size of 50–200 nm, displaying a spike shaped structure. Fig. 2 shows the cross section of multi-walled VO$_x$-NTs and its magnified interlamellar microstructure. We can see that VO$_x$-NTs, which form through the curl mechanism [18], are composed of alternately arranged VO$_x$ layers and dodecylamine templates. Further enlarged cross sectional view indicates VO$_x$ layer consists of two sheets of VO$_5$ square pyramids with apexes pointing toward opposite directions and joined by VO$_4$ tetrahedra [19]. The protonated dodecylamine cations (C$_{12}$H$_{25}$NH$_3^+$) bind electrostatically to the VO$_x$ layers [20], which forms the alternately intercalated structure because the protonated organic template is positively charged and the VO$_x$ layer is negatively charged. However, this binding force is not so strong.

XPS technique was employed to identify the element component of VO$_x$-NTs and analyze the content of vanadium element with
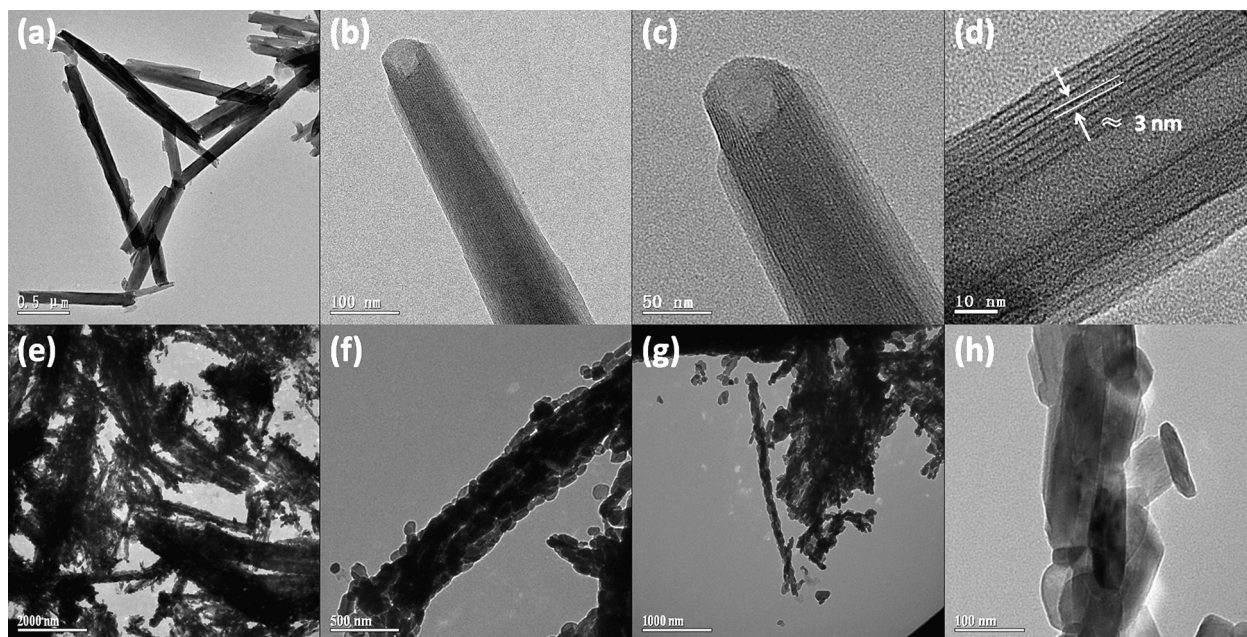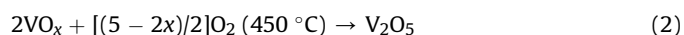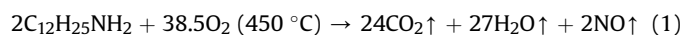
Fig. 1. TEM images of VO_x-NTs (a–d) and V_2O_5-NS (e–h) at different magnifications.

different valence states. The XPS general spectrum of VO_x-NTs is given in Fig. 3(a). The weak N_{1s} peak at about 400 eV originates from $-C-NH_2$ group within the protonated dodecylamine templates ($C_{12}H_{25}NH_3^+$). Fig. 3(b) presents the V_{2p} region of XPS

Fig. 2. Cross-sectional view and magnified interlamellar microstructure of VO_x-NTs.

spectrum, which includes the $V_{2p3/2}$ and $V_{2p1/2}$ peaks, and $V_{2p3/2}$ peak can be divided into two peaks at the binding energies of 517.3 and 516.1 eV which are ascribed to V^{5+} and V^{4+}, respectively [21]. As shown in Fig. 3(b), XPS Peak4.1 software was applied to fit the experimental data and ascertain the ratio of V^{5+}/V^{4+} in VO_x-NTs through the calculation of V^{5+} peak area/V^{4+} peak area. The fitted result illustrates that the ratio of V^{5+}/V^{4+} in VO_x-NTs is 0.92, that is, V^{5+} and V^{4+} account for 48% and 52%, respectively. As we know, the vanadium valence decreases with the insertion of lithium ions during electrochemical process. So, the higher vanadium valence means the greater potential for lithium ions insertion. In the sintering process, mixed-valence VO_x-NTs will be oxidized, recrystallized and finally transformed into high-valence V_2O_5-NS, leading to the higher specific capacity.

Fig. 4 gives schematic diagram of V_2O_5-NS formation during sintering. The protonated dodecylamine, which binds electrostatically to the VO_x layer, is easily decomposed in oxygen on heat treatment. Owing to the special nanosized multi-walled tubular structure possessed by VO_x-NTs, the oxidative decomposition of dodecylamine templates under oxygen atmosphere through sintering causes the collapse and recrystallization of VO_x layers within VO_x-NTs, leading to the appearance of small V_2O_5 nanocrystals. The sintering process can be described by the following chemical reaction equations:

$$2C_{12}H_{25}NH_2 + 38.5O_2 \ (450\ ^\circ C) \rightarrow 24CO_2\uparrow + 27H_2O\uparrow + 2NO\uparrow \quad (1)$$

$$2VO_x + [(5-2x)/2]O_2 \ (450\ ^\circ C) \rightarrow V_2O_5 \quad (2)$$

The nanotube and nanospike shaped morphologies of VO_x-NTs (Fig. 5a and b) and V_2O_5-NS (Fig. 5c and d) are confirmed again by SEM images in Fig. 5. It is obvious that both of the samples exhibit cross-linked network which provides high electroactive surface area and numerous electrolyte-filled channels, facilitating lithium ion diffusion in the materials. In addition, structural change associated with lithium intercalation/deintercalation can be easily relaxed in the small V_2O_5 nanocrystals of V_2O_5-NS. There are several reasons so that we need to conduct sintering treatment on as-prepared VO_x-NTs: (1) Dodecylamine template has no
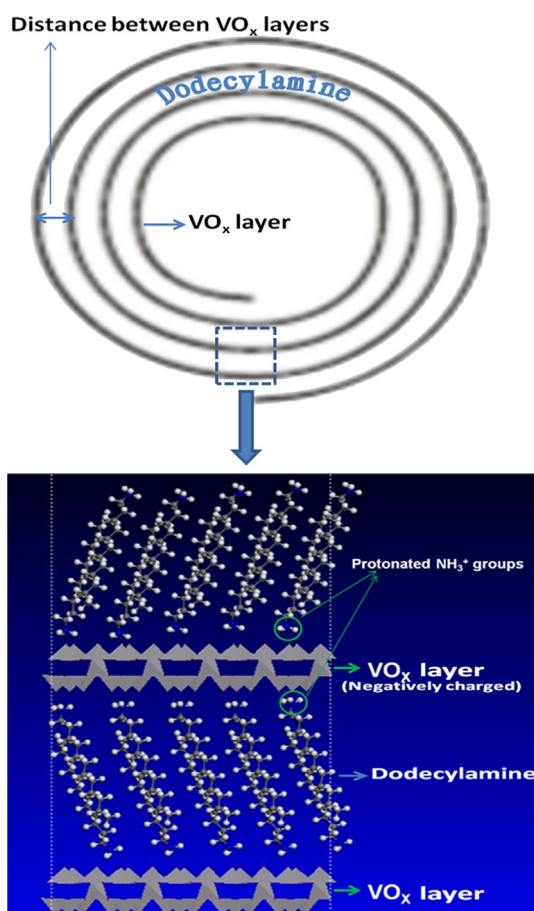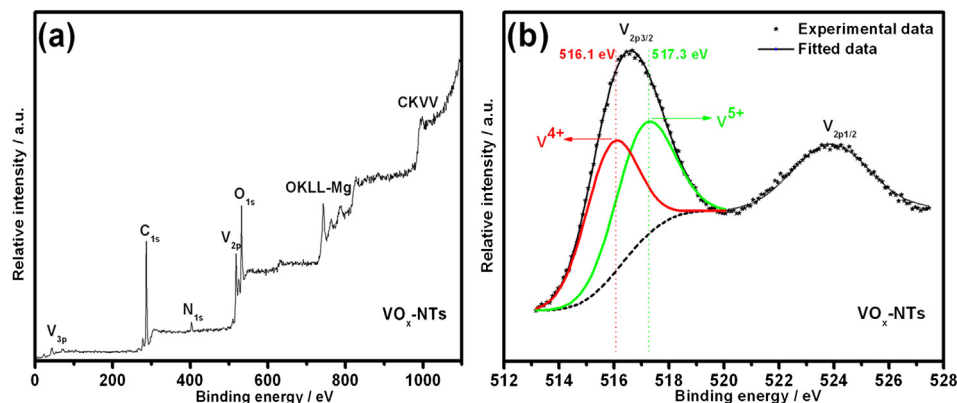
Fig. 3. XPS general spectrum and V_{2p} region of VO_x-NTs.

contribution to electrochemical performance and will degrade cathode material due to its decomposition in electrochemical process. Furthermore, the removal of organic templates can increase the utilization rate of cathode. (2) Vanadium atoms in VO_x-NTs are in the mixed valence state of V^{4+}/V^{5+}, which would limit the maximum capacity of vanadium pentoxide cathode material. (3) The poor crystallinity of VO_x-NTs isn't conducive to its cyclic stability.

The structure of VO_x-NTs and V_2O_5-NS was examined by XRD measurements. As presented in Fig. 6, VO_x-NTs display a set of ($00l$) diffraction peaks including (001), (002) and (003) peaks at small-angle region, which correspond to its lamellar structure. The position (3.17°) of (001) peak is utilized to calculate the distance between VO_x layers within VO_x-NTs [22]. According to Bragg's law, this value is 2.79 nm and close to the result of TEM observation. Another set of enlarged ($hk0$) peaks consisting of (110), (210), (310) peaks, and so on at large-angle region (15°–50°), as illustrated in Fig. 6 (inset), reflect the two-dimensional structure of VO_x layers. V_2O_5-NS exhibits a series of characteristic diffraction peaks (200), (001), (101), (110), (400), etc. which are consistent with those of crystalline V_2O_5 powder (space group: $Pmmn$, $a = 11.516$ Å, $b = 3.566$ Å, $c = 4.372$ Å), and no other peaks are detected, indicating the high purity of V_2O_5 nanocrystals. Through calculation based on Scherrer formula, the average grain size of V_2O_5 nanocrystals is ∼70 nm which is in good agreement with TEM and SEM observations.

Fig. 7 gives the TG-DSC curves of VO_x-NTs in air. Weight loss of 2.8% from the room temperature to about 200 °C is assigned to the thermal evaporation of absorbed water molecules. The thorough oxidative decomposition of organic templates for VO_x-NTs is completed at 411 °C, causing total 39.2% of weight loss which would describe the approximate content of organic templates in VO_x-NTs.

Two exothermic peaks at 270 °C and 396 °C can mainly be ascribed to the decomposition of dodecylamine and recrystallization of VO_x layers, respectively. It can be seen that VO_x-NTs contain a large part of organic templates which has no contribution to electrochemical capacity.

FTIR spectroscopy was performed to determine whether any organic templates are left after sintering. As seen from Fig. 8, the absorption peaks at 721, 1465, 2850, and 2920 cm^{-1}, which can be assigned to the various bending and stretching modes of C–H vibrations in dodecylamine for VO_x-NTs [23], are totally disappeared for V_2O_5-NS, indicating the complete removal of dodecylamine templates. For both of the samples, the characteristic peaks near 1000 cm^{-1} (1002 and 1016 cm^{-1}), ranging from 700 to 900 cm^{-1} (785 and 829 cm^{-1}) and below 700 cm^{-1} (496, 575, 487 and 631 cm^{-1}) correspond to the stretching vibration of terminal oxygen bonds (V=O), the vibration of doubly coordinated oxygen bonds, and the asymmetric and symmetric stretching vibrations of triply coordinated oxygen bonds in vanadium oxide, respectively [24]. The shifting of corresponding coordinated oxygen bonds may be caused by the lattice distortion and microscopic stress variation in coordination geometry [25]. Two peaks at 1620 and 3425 cm^{-1} are attributed to H–O stretching and H–O–H bending vibration modes [26].

Systematic electrochemical tests about VO_x-NTs and V_2O_5-NS were carried out to demonstrate their electrochemical properties. As shown in Fig. 9(a), only the first discharge curve of V_2O_5-NS displays four obvious plateaus at 3.38 V, 3.19 V, 2.27 V and 2.03 V, corresponding to the phase transitions of α-$Li_xV_2O_5$ ($x < 0.01$) to ε-$Li_xV_2O_5$ ($0.35 < x < 0.7$), ε-$Li_xV_2O_5$ to δ-$Li_xV_2O_5$ ($x < 1$), δ-$Li_xV_2O_5$ to γ-$Li_xV_2O_5$ ($x > 1$) and γ-$Li_xV_2O_5$ to ω-$Li_xV_2O_5$ ($x > 2$) respectively during lithium ion intercalation process [27]. After that both of the samples exhibit smooth discharge curves, reflecting their
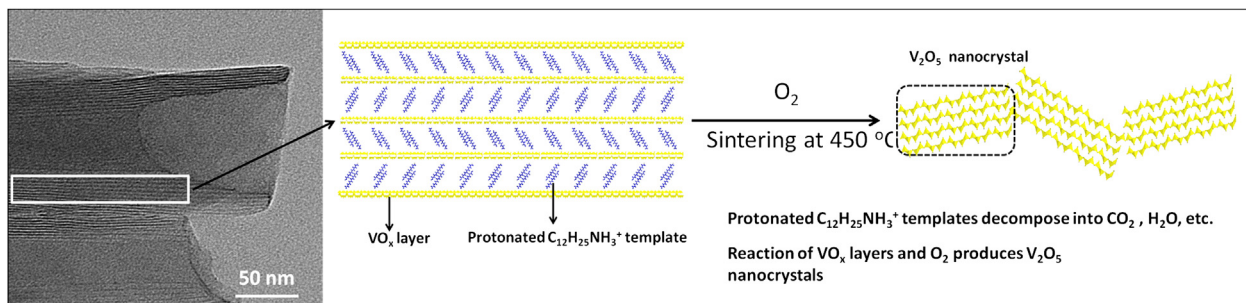

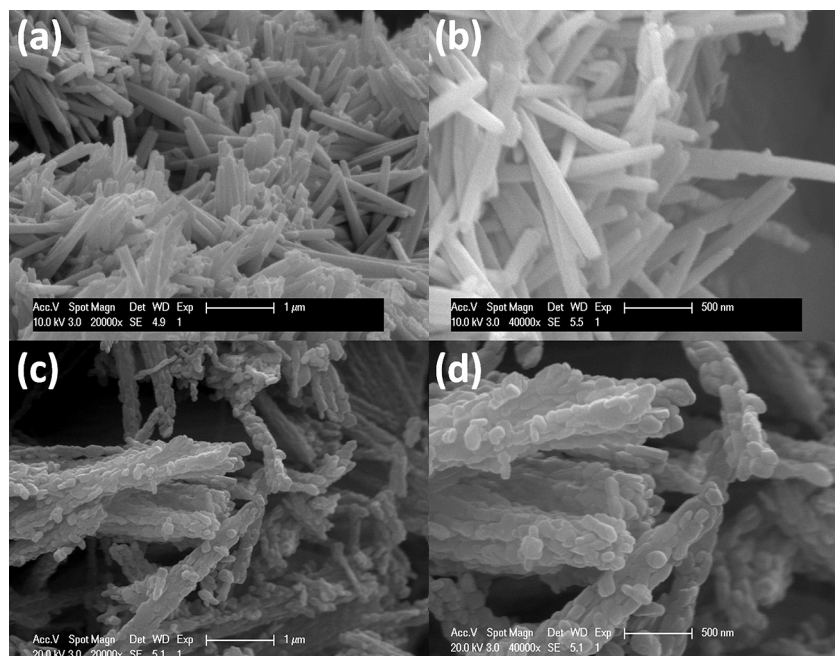Fig. 4. Schematic diagram showing the formation of V_2O_5 nanocrystals during sintering.

Fig. 5. SEM images of VO$_x$-NTs (a,b) and V$_2$O$_5$-NS (c,d) at different magnifications.

amorphous features as cathode materials [28]. The orthorhombic V$_2$O$_5$-NS cathode reported here is charged/discharged at a wide voltage window (1.5–4 V), which will result in high specific capacity. However, the phase transitions of orthorhombic V$_2$O$_5$-NS are irreversible at such a deep discharge. So, the repeated charge/discharge plateaus would not be found in the subsequent cycles. Normally, if we test V$_2$O$_5$-based electrode at a narrow voltage window, the well-repeated charge/discharge plateaus also can be observed, but the specific capacity obtained will be greatly reduced. As it can be seen from the initial discharge curves of V$_2$O$_5$-NS in Fig. 9(a), a large part of discharge capacity is distributed between 1.5 and 2.5 V. Cyclic voltammogram in Fig. 9(b) shows the first to fourth cycles of two samples. In order to research the Li$^+$ insertion/extraction characteristic of these nanostructured cathode materials under high power condition, a relatively high scan rate (2 mV s^{-1})

was applied in CV tests. It can be seen that V$_2$O$_5$-NS shows larger peak area and more stable peak shape than VO$_x$-NTs, except for the initial cycle which presents three pronounced cathodic peaks related with its irreversible multi-step intercalation of lithium ion in the first discharge process [29]. It manifests V$_2$O$_5$-NS possesses higher capacity and better cycling performance compared with VO$_x$-NTs [30]. To investigate the electrochemical behavior of V$_2$O$_5$-NS more accurately, a CV test was performed at low scan rate of 0.1 mV s^{-1} as illustrated in Fig. 9(c). As can be observed, two downward cathodic peaks (Li$^+$ insertion) at 3.34 and 3.12 V in initial cycle match well with the discharge plateaus at 3.38 and 3.19 V in Fig. 9(a), respectively, and the other two peaks at 2.16 and 1.83 V basically correspond to the discharge plateaus at 2.27 and 2.03 V in Fig. 9(a), respectively. We could find that a slight shift of cathodic peak positions at low-voltage region occurs, which is mainly caused by the polarization of electrode materials near the cut-off voltage. It is noteworthy that an upward anodic peak at
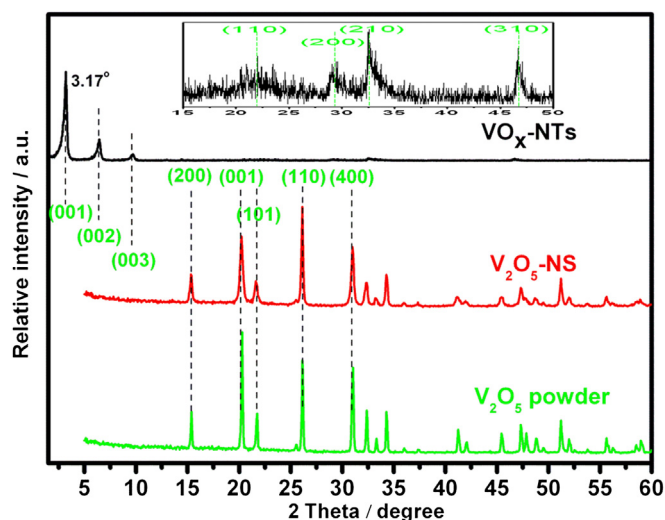

Fig. 6. XRD patterns of raw V$_2$O$_5$ powder, VO$_x$-NTs and V$_2$O$_5$-NS (inset: enlarged XRD pattern for VO$_x$-NTs between 15° and 50°).
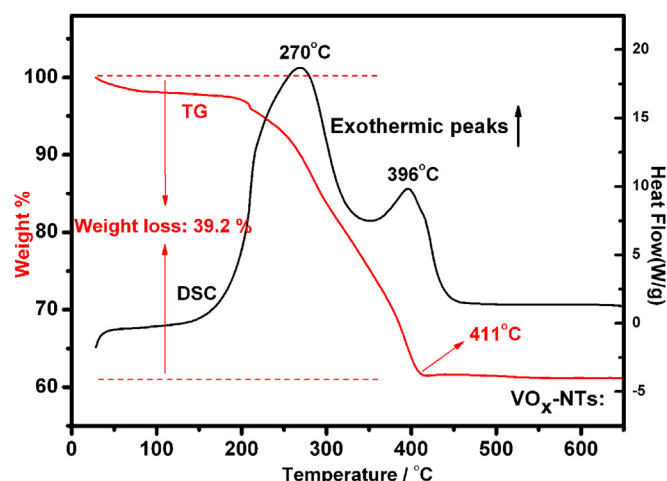
Fig. 7. TG-DSC curves of VO$_x$-NTs in air.
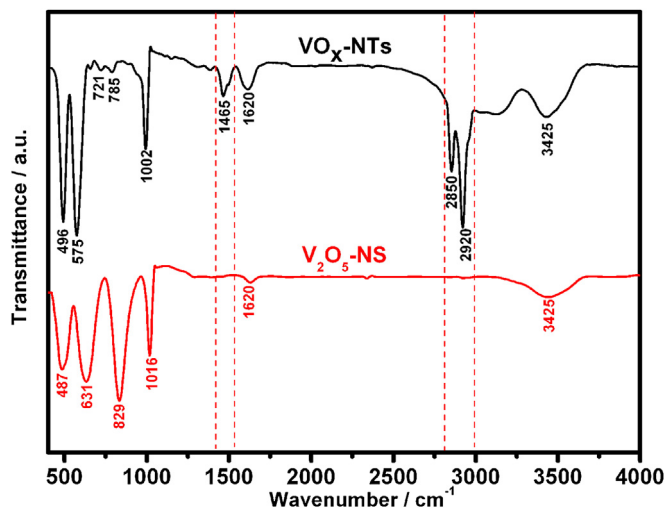
Fig. 8. FTIR spectra of VO$_x$-NTs and V$_2$O$_5$-NS.

3.45 V appears at the beginning of cycle, which results from the extraction of lithium ions previously intercalated into the cathode materials due to a small quantity of self-discharge of coin sell. The following second and third CV curves almost completely overlap each other, indicating the good cyclability of V$_2$O$_5$-NS cathode materials.

As observed from galvanostatic cycles in Fig. 10, V$_2$O$_5$-NS delivers the initial specific capacity of 427, 409, 392 mA h g^{-1} at the current density of 50, 100 and 150 mA g^{-1}, respectively, and after 50 cycles it remains the capacity of 219, 210 and 197 mA h g^{-1}. The corresponding values for VO$_x$-NTs are 253, 242 and 225 mA h g^{-1} at 50, 80 and 100 mA g^{-1}, respectively, and after 50 cycles there is only about 33 mA h g^{-1} left. For theoretical analysis, if we calculate the specific capacity of VO$_x$-NTs only based on the content of electroactive VO$_x$ layers, the initial specific capacity of VO$_x$-NTs would be 416, 398 and 370 mA h g^{-1} at the current density of 50, 80 and 100 mA g^{-1}, respectively, and after 50 cycle ∼54 mA h g^{-1} was left for all cases. By comparison, these values are also lower than those of V$_2$O$_5$-NS at the same conditions. However, in practical application, it is unreasonable to consider only the mass of VO$_x$ layers within VO$_x$-NTs, because the dodecylamine template is integrated with VO$_x$ layer into a whole. The rapid capacity decay of VO$_x$-NTs maybe caused by the decomposition of dodecylamine and its severe contamination to electrolyte. It is worth noting that there is a sharp decrease in the capacity of V$_2$O$_5$-NS after initial galvanostatic cycle. This is because some Li$^+$ ions would permanently insert into V$_2$O$_5$ matrix at deep discharge condition (below 2 V) in the first lithiation process [31]. It can be concluded that nanospike shaped V$_2$O$_5$-NS, which is composed of interconnected V$_2$O$_5$ nanocrystals and free of organic templates, possesses high specific capacity, superior cycling performance and good rate capability. The prepared V$_2$O$_5$-NS here with amorphous feature and good ion intercalation characteristic can be used as an important component for the synthesis of supercapacitor materials, if it could combine with nanostructured carbon materials with high specific surface area and superior conductivity, because V$_2$O$_5$-NS would provide a large amount of pseudocapacitance in supercapacitor application.

To investigate the Li$^+$ insertion mechanism at the cathode/electrolyte interface and evaluate the diffusion of Li$^+$ within the bulk of cathode material, EIS measurements were carried out for VO$_x$-NTs and V$_2$O$_5$-NS electrodes. As illustrated in Fig. 11(a), Nyquist plots derived from EIS tests at the state of charge of 3 V show a depressed semicircle in high-frequency region and a sloped line in low-
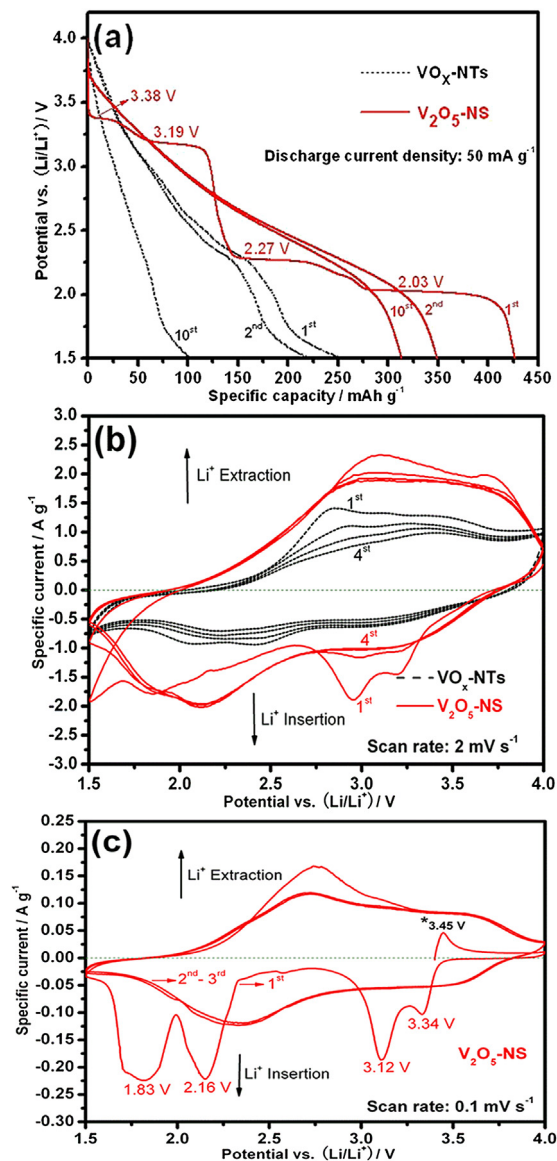

Fig. 9. The first, second and tenth discharge curves (a) of VO$_x$-NTs and V$_2$O$_5$-NS at the discharge current density of 50 mA g^{-1}, cyclic voltammograms (b) of the two samples showing the first to fourth cycles at the scan rate of 2 mV s^{-1} and (c) CV curves of V$_2$O$_5$-NS showing the initial three cycles under low scan rate of 0.1 mV s^{-1} between 1.5 and 4 V.

frequency region, which corresponds to the charge transfer reaction at the cathode/electrolyte interface and Warburg impedance associated with Li$^+$ ions diffusion in cathode material, respectively [32,33]. Generally, the smaller the diameter of the semicircle is, the smaller the charge transfer resistance will be [34]. We further fit the plots using built equivalent circuit (inset), in which R_e presents the electrolyte resistance, R_{ct} stands for the charge transfer resistance, CPE is a constant phase-angle element, and W_o is the Warburg impedance. The obtained R_{ct} of V$_2$O$_5$-NS is obviously smaller than that of VO$_x$-NTs as listed in Table 1, which demonstrates the transfer and diffusion of Li$^+$ ions through the cathode/electrolyte interface of V$_2$O$_5$-NS is more easy than VO$_x$-NTs. The large charge transfer resistance for VO$_x$-NTs is due to the existence of plentiful organic templates that is not electroactive.

As mentioned early, Nyquist plots display an oblique line at the low frequency region (∼1 Hz–0.01 Hz). When we use the value of real impedance (Z_{re}, refer to Eq. (3)) [35] as the function of the inverse
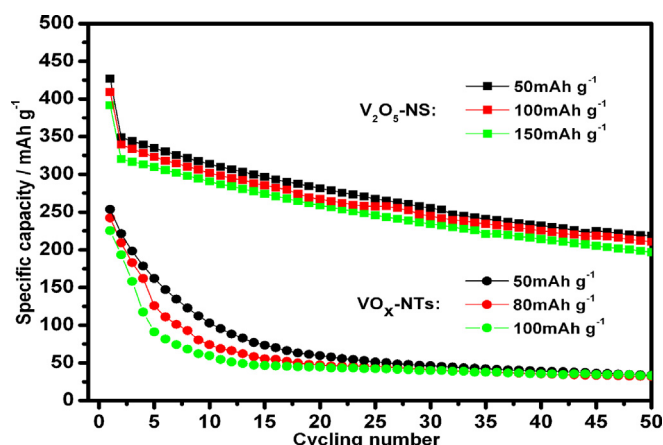
Fig. 10. Galvanostatic cycles of VO$_x$-NTs and V$_2$O$_5$-NS under different current density between 1.5 and 4 V.

of square root of angular frequency ($\omega^{-1/2}$) at the low frequency region, a perfect linear relationship between Z_{re} and $\omega^{-1/2}$ will be acquired as shown in Fig. 11(b). According to Eq. (3), the slope (A_w) of the straight line in Fig. 11(b) is Warburg impedance coefficient, the
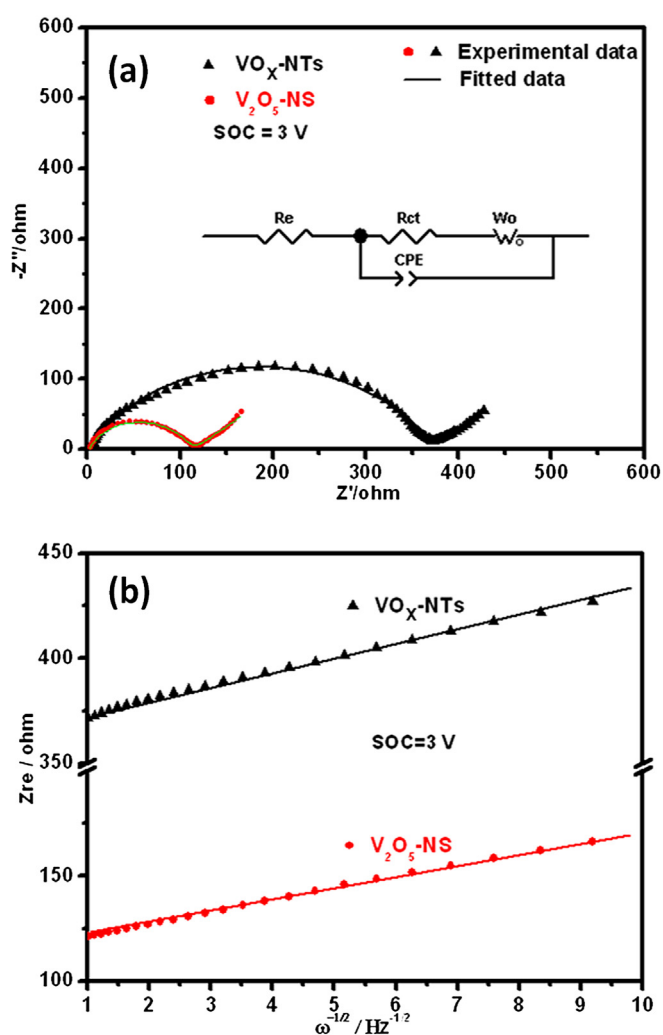
Table 1
The fitted electrolyte resistance (R_e), charge transfer resistance (R_{ct}) and Warburg impedance coefficient (A_w) values for the two samples at the state of charge (SOC) of 3 V.

Samples	R_e (ohm)	R_{ct} (ohm)	A_w (Ω cm^2 s$^{-1/2}$)
VO$_x$-NTs	2.413	368.2	7.12
V$_2$O$_5$-NS	2.166	103.8	5.18

reciprocal of whose squared value is proportional to the lithium ion diffusion coefficient D_{Li} (refer to Eq. (4)) [36]. So, the value of Warburg impedance coefficient (A_w) can be used to indirectly speculate the diffusion of Li$^+$ within cathode materials. The calculated values of A_w for VO$_x$-NTs and V$_2$O$_5$-NS are listed in Table 1. Both of the samples show the small Warburg impedance coefficient because of their special nanostructures, which means favorable lithium ion diffusion condition within these nanostructured materials. Herein, V$_2$O$_5$-NS shows smaller A_w value compared to VO$_x$-NTs for the sake of the removal of organic templates.

$$Z_{re} = R_e + R_{ct} + A_w\omega^{-1/2} \tag{3}$$

$$D_{Li} \propto 1/A_w^2 \tag{4}$$

The results of above EIS measurements can offer auxiliary explanations for the superior electrochemical performance of V$_2$O$_5$-NS, especially its good rate capability.

4. Conclusions

A novel vanadium pentoxide nanospike (V$_2$O$_5$-NS) composed of interconnected V$_2$O$_5$ nanocrystals (50–200 nm) is prepared through post sintering treatment of hydrothermally synthesized vanadium oxide nanotubes (VO$_x$-NTs) under mixed atmosphere of nitrogen and oxygen. It delivers excellent specific capacity (initial capacity of 427 mA h g^{-1} at 50 mA g^{-1}) and good cycling performance (219 mA h g^{-1} after 50 cycles at 50 mA g^{-1}) as cathode materials for lithium ion batteries due to the increased electroactive surface area created by the nanospiked configuration of V$_2$O$_5$-NS. Furthermore, V$_2$O$_5$-NS also displays outstanding rate capability (392 mA h g^{-1} for the first cycle and 197 mA h g^{-1} after 50 cycles at 150 mA g^{-1}), which can be attributed to short lithium ion diffusion pathway within electroactive V$_2$O$_5$-NS, lower charge transfer resistance through electrolyte/V$_2$O$_5$-NS interface and good Li$^+$ diffusion into the bulk of cathode material. This novel V$_2$O$_5$-NS cathode material can be a promising candidate for high performance lithium ion batteries. The facile technique used in this work is novel and effective to fabricate nanostructured vanadium oxide.

Fig. 11. Nyquist plots (a) of VO$_x$-NTs and V$_2$O$_5$-NS with 5 mV amplitude of AC signal at the state of charge of 3 V (inset: equivalent circuit used for fitting the Nyquist plots), and relationship (b) between the real impedance (Z_{re}) and the inverse of square root of angular frequency ($\omega^{-1/2}$) at the low frequency region.

References

[1] J.M. Tarascon, M. Armand, Nature 414 (2001) 359–367.
[2] J. Hassoun, P. Reale, B. Scrosati, J. Mater. Chem. 17 (2007) 3668–3677.
[3] Y.L. Cheah, N. Gupta, S.S. Pramana, V. Aravindan, G. Wee, M. Srinivasan, J. Power Sources 196 (2011) 6465–6472.

[4] Y. Wang, G.Z. Cao, Adv. Mater. 20 (2008) 2251–2269.
[5] Y. Wang, K. Takahashi, K. Lee, G.Z. Cao, Adv. Funct. Mater. 16 (2006) 1133–1144.
[6] A.M. Kannan, A. Manthiram, J. Electrochem. Soc. 150 (2003) A990–A993.
[7] J. Muster, G.T. Kim, V. Krstic, J.G. Park, Y.W. Park, S. Roth, M. Burghard, Adv. Mater. 12 (2000) 420–424.
[8] B.B. Owens, S. Passerini, W.H. Smyrl, Electrochim. Acta 45 (1999) 215–224.
[9] G. Gregoire, N. Baffier, A.K. Harari, J.C. Badot, J. Mater. Chem. 8 (1998) 2103–2108.
[10] M. Macias, A. Chacko, J.P. Ferraris, K.J. Balkus Jr., Microporous Mesoporous Mater. 86 (2005) 1–13.
[11] A.Q. Pan, J.G. Zhang, Z. Nie, G.Z. Cao, B.W. Arey, G.S. Li, S.Q. Liang, J. Liu, J. Mater. Chem. 20 (2010) 9193–9199.
[12] C.C. Hu, K.H. Chang, C.M. Huang, J.M. Li, J. Electrochem. Soc. 156 (2009) D485–D489.
[13] C.V.S. Reddy, J. Wei, Z. Quan-Yao, D. Zhi-Rong, C. Wen, S. Mho, R.R. Kalluru, J. Power Sources 166 (2007) 244–249.
[14] C. Ban, N.A. Chernova, M.S. Whittingham, Electrochem. Commun. 11 (2009) 522–525.
[15] L.Q. Mai, L. Xu, C.H. Han, X. Xu, Y.Z. Luo, S.Y. Zhao, Y.L. Zhao, Nano Lett. 10 (2010) 4750–4755.
[16] X.W. Zhou, G.M. Wu, G.H. Gao, J.C. Wang, H.Y. Yang, J.D. Wu, J. Shen, B. Zhou, Z.H. Zhang, J. Phys. Chem. C 116 (2012) 21685–21692.
[17] B. Alonso, J. Livage, J. Solid State Chem. 148 (1999) 16–19.
[18] H.-J. Muhr, F. Krumeich, U.P. Schonholzer, F. Bieri, M. Niederberger, L.J. Gauckler, R. Nesper, Adv. Mater. 12 (2000) 231–234.
[19] X. Wang, L. Liu, R. Bontchev, A.J. Jacobson, Chem. Commun. 9 (1998) 1009–1010.
[20] L.I. Vera-Robles, A. Campero, J. Phys. Chem. C 112 (2008) 19930–19933.
[21] X. Liu, G. Xie, C. Huang, Q. Xu, Y. Zhang, Y. Luo, Mater. Lett. 62 (2008) 1878–1880.
[22] J. Li, L.F. Zheng, K.F. Zhang, X.Q. Feng, Z.X. Su, J.T. Ma, Mater. Res. Bull. 43 (2008) 2810–2817.
[23] M. Malta, G. Louarn, N. Errien, R.M. Torresi, J. Power Sources 156 (2006) 533–540.
[24] A. Surca, B. Orel, Electrochim. Acta 44 (1999) 3051–3057.
[25] Y.J. Liu, J.L. Schindler, D.C. DeGroot, C.R. Kannewurf, W. Hirpo, M.G. Kanatzidis, Chem. Mater. 8 (1996) 525–534.
[26] L.J. Mao, C.Y. Liu, Mater. Res. Bull. 43 (2008) 1384–1392.
[27] N.A. Chernova, M. Roppolo, A.C. Dillon, M.S. Whittingham, J. Mater. Chem. 19 (2009) 2526–2552.
[28] C.Q. Feng, S.Y. Wang, R. Zeng, Z.P. Guo, K. Konstantinov, H.K. Liu, J. Power Sources 184 (2008) 485–488.
[29] M. Broussely, F. Perton, J. Labat, R.J. Staniewicz, A. Romero, J. Power Sources 43 (1993) 209–216.
[30] C.Q. Feng, S.Y. Chew, Z.P. Guo, J.Z. Wang, H.K. Liu, J. Power Sources 174 (2007) 1095–1099.
[31] S.H. Ng, T.J. Patey, R. Buechel, F. Krumeich, J.Z. Wang, H.K. Liu, S.E. Pratsinis, Phys. Chem. Chem. Phys. 11 (2009) 3748–3755.
[32] L. Jiao, H. Yuan, Y. Wang, J. Cao, Y. Wang, Electrochem. Commun. 7 (2005) 431–436.
[33] A.Y. Shenouda, H.K. Liu, J. Power Sources 185 (2008) 1386–1391.
[34] Y. Liu, X. Zhou, Y. Guo, Electrochim. Acta 54 (2009) 3184–3190.
[35] J. Yan, W. Yuan, Z.Y. Tang, H. Xie, W.F. Mao, L. Ma, J. Power Sources 209 (2012) 251–256.
[36] B. Jin, E.M. Jin, K.-H. Park, H.-B. Gu, Electrochem. Commun. 10 (2008) 1537–1540.